Resistance of single domain walls in half-metallic CrO₂ epitaxial nanostructures

Lijuan Qian, Shiyu Zhou, Kang Wang, and Gang Xiao*

Department of Physics, Brown University, Providence, Rhode Island 02912, USA

Abstract

Magnetic domain structures are active electron transport agents and can be used to

induce large magnetoresistance (MR), particularly in half-metallic solids. We have

studied the excess resistance induced by a single magnetic domain wall in a one-

dimensional half-metallic CrO2 nanoscale conductor with a built-in constriction whose

channel width (d) ranging from 30 to 200 nm. We have uncovered a large size effect of

d on the domain wall resistance (DWR), which scales with d as $d^{-1.87\pm0.32}$. Accordingly,

we predict that the MR ratio of a simple CrO₂ nanowire impregnated with a constriction

at a 150 nm² cross-section could reach 100%. This large MR far exceeds that of a

conventional ferromagnetic nanowire, confirming the role of half metallicity on

enhanced magneto transport.

*Email: Gang Xiao@Brown.edu

1

1. Introduction

It is known that spin textures such as domain walls (DWs) can induce excess resistivity in ferromagnetic materials [1-6]. According to the Levy-Zhang model, the excess resistivity originates from the mixing of two spin current channels within non-homogeneous spin states [1]. Research on domain-wall resistance (DWR) and electron transport in spin textures benefit its potential application in spintronic devices [7,8]. Half-metallic ferromagnets with 100% spin polarization are ideal systems to investigate DWR, as their infinitely large spin asymmetry manifests prominently in the magneto-transport. Among them, half metal CrO₂ has been extensively studied, and its half metallicity has been confirmed through various experimental techniques [9-12]. Previously, we have reported for the first time the observation of the excess resistance induced by a single DW in CrO₂ [13]. We estimated through magneto-transport measurements and micromagnetic simulations that the DW resistivity ratio $(\frac{\Delta \rho_{\rm DW}}{\rho_0})$ in CrO₂ is in the range of 1.3% to 13.2% at the temperature of 5 K. $\Delta \rho_{DW}$ is the excess resistivity induced by a single DW and ρ_0 is the resistivity of the CrO₂ in the single-domain state [13]. Afterwards, we investigated the resistivity induced by general spin textures besides DWs. We uncovered the correlation between the magnetoresistance (MR) in CrO₂ and the spin curvature which characterizes the spatial nonuniformity of spins [2]. From the empirical correlation between the excess resistivity and spin curvature of spin textures, we estimated the DWR in CrO₂ which is consistent with our previous measurement results [2,13]. The spin curvature induced MR can be explained by the Levy-Zhang model and the magnitude of the excess resistivity of a spin texture is determined by its spin configuration and the spin asymmetry parameter $(\rho_{\uparrow}/\rho_{\downarrow})$ of the material. These studies provide a guidance for us to manipulate the DW configuration and achieve a large

DWR by modifying CrO₂ nanostructures, which is of great interest to both fundamental research and spintronic applications.

In this work, we investigate the DWR in CrO_2 epitaxial nanostructures with varying structure sizes and explore the size effects on the DW configuration and corresponding DWR. The single DWs are created and annihilated in nanostructures with an asymmetrical weak link, which we call *nano-constriction* where the constriction width d varies from 30 to 200 nm. The DWR is substantially enhanced when the constriction width d reduces, which is possibly because the electrons cannot accommodate the spin changes inside the nano-constrictions when the constriction size is decreased to tens of nanometers. The DWR scales with $S^{-1.87\pm0.32}$ where S is the cross-sectional area of the constriction. Based on this power law, a large MR of 100 % is expected when S is reduced to 150 nm², e.g., in a 10 nm-thick and 15 nm-wide constriction. The DMR value of CrO_2 is much larger than that of other non-half-metallic magnetic solids such as Ni and NiFe at comparable cross-sectional areas.

2. Experimental

We fabricated epitaxial CrO_2 nanostructures using the techniques of electron-beam lithography, chemical vapor deposition (CVD), and selective area growth (SAG) without post-deposition patterning. The CrO_2 nanostructures are grown on TiO_2 single crystal substrates. The detailed fabrication process can be found in our previous studies [2,9,13]. Our earlier experiments have shown that the CrO_2 thin films deposited this way exhibit a spin polarization of 0.96 ± 0.01 at 1.85 K [9]. In this work, we studied a nanowire with a built-in weak link which we call nano-constriction with a variable constriction width. We were able to generate or annihilate

a single DW located near the constriction. We then studed the DW configuration and DWR through the complementary micromagnetic simulations and magneto-transport measurements.

Micromagnetic simulation is an effective tool to reveal magnetization states in magnetic nanostructures. For every structure studied in this work, we performed micromagnetic simulation using mumax³, a GPU-accelerated program developed at Ghent University [14]. The software simulates the time and spatial evolution of spin configurations based on the Landau-Lifshitz micromagnetic formalism using the method of finite difference discretization. We obtain the equilibrium magnetization states in the CrO₂ nanostructures under various external magnetic fields by minimizing the total free energy including four energy terms.

The Zeeman energy originates from the interaction between the magnetization and external field. The energy density is expressed as $\varepsilon_{\text{zeeman}} = -\vec{M} \cdot \vec{B}_{\text{ext}}$, where $\vec{M} = M_{\text{S}} \hat{m}$ is the magnetization vector, $M_{\text{S}} = 640$ emu/cm³ is the saturation magnetization experimentally obtained at 10 K [15], \hat{m} is the unit magnetization vector, and \vec{B}_{ext} is the external magnetic field.

The exchange energy arises from the exchange coupling between neighboring spins, which is responsible for the ferromagnetic ordering. The energy density is $\varepsilon_{\rm exchange} = -\frac{1}{2}\vec{M}$. $\vec{B}_{\rm exch}$, where $\vec{B}_{\rm exch} = 2\frac{A_{\rm ex}}{M_{\rm S}}\Delta\hat{m}$ is the effective field due to the Heisenberg exchange interaction, and $A_{\rm ex}$ is the exchange constant. Based on the Curie temperature ($T_{\rm C} = 398~{\rm K}$) of CrO₂, the exchange constant $A_{\rm ex}$ is estimated to be $4.6 \times 10^{-7}~{\rm erg/cm}$ [15].

The demagnetization energy, $\varepsilon_{\rm demag} = -\frac{1}{2} \vec{M} \cdot \vec{B}_{\rm demag}$, accounts for the shape anisotropy, where $\vec{B}_{\rm demag}$ is the demagnetization field. Finally, the magnetocrystalline anisotropy energy is determined by the crystal structure of the material. In 100 nm-thick CrO₂

epitaxial films, the uniaxial anisotropy axis is along the [001] direction [15]. The corresponding energy density is $\varepsilon_{\rm anis} = -\frac{1}{2} \vec{M} \cdot \vec{B}_{\rm anis}$, where $\vec{B}_{\rm anis} = \frac{2K_{\rm u1}}{M_{\rm sat}} (\hat{u} \cdot \hat{m}) \hat{u}$ is the effective anisotropy field, \hat{u} is the unit vector denoting the uniaxial anisotropy axis, and $K_{\rm u1}$ is the uniaxial anisotropy constant which has been previously measured as $9.2 \times 10^4 \, {\rm erg/cm^3}$ [15]. Table I summarizes the parameters adopted in our simulations. The magnetic films are discretized into cells with the cell size of 4 nm which is smaller than the Bloch wall width $\sqrt{\frac{A_{\rm ex}}{K_{\rm u1}}} = 22 \, {\rm nm}$ and the exchange length $\sqrt{\frac{A_{\rm ex}}{K_{\rm d}}} = \sqrt{\frac{A_{\rm ex}}{2\pi M_{\rm s}^2}} = 4.2 \, {\rm nm}$ [16] to ensure simulation accuracy.

Table I. Physical parameters used in micromagnetic simulations

Parameter	Value	Reference
Saturation magnetization M_s	640 emu/cm ³	[15]
Exchange constant A_{ex}	$4.6 \times 10^{-7} \text{erg/cm}$	[15]
Uniaxial anisotropy constant K_{u1}	$9.2 \times 10^4 \text{erg/cm}^3$	[15]
Cell size	4 nm	N/A
Gilbert damping coefficient α	0.023	[17]

3. Results and Discussion

Figure 1(a) shows the schematic diagram of the nanostructure with an asymmetrical weak link. The longitudinal axis of the structure, denoted as the x axis, is along the [001] direction, which is the magnetocrystalline easy axis in the 100 nm-thick CrO_2 epitaxial films [15]. The transverse axis of the structure, denoted as the y axis, is along the [010] direction, which is the hard axis. The width of the main lead of the structure is one micron, while the constriction width, d, varies (d = 30, 50, 120,and 200 nm). The boundaries on the left and right side of the constriction form wedges with angles of 60° and 15° , respectively, relative to the x axis. The

asymmetry is essential to introducing the DW state in the vicinity of the constriction through the external magnetic field. Moreover, varying the constriction width is essential to modifying the DW configuration near the constriction where the demagnetization energy plays an important role in determining the magnetization state.

Due to the shape anisotropy, the magnetic field required to reverse magnetization, which we denote as the reversing field ($B_{\rm rev}$), is different for spins on the left and right side of the constrictions. In our design, $|B_{\rm rev}({\rm left})| < |B_{\rm rev}({\rm right})|$. When the applied field ($B_{\rm app}$) is in between the two reversing fields, i.e., $|B_{\rm rev}({\rm left})| < |B_{\rm app}| < |B_{\rm rev}({\rm right})|$, the magnetization on the left is along the opposite direction to the magnetization on the right side of the constriction. Therefore, a DW is formed near the constriction. Far away from the constriction, four leads are designed for the 4-probe measurement of the resistivity of the nanostructures. Figure 1(b) is a representative scanning electron microscopy (SEM) image of the nanostructure with d=50 nm, with the dark region as the epitaxial ${\rm CrO_2}$ nanostructure and light region as ${\rm SiO_2}$. From the SEM image, we analyze the roughness of the edges of the nanostructure and conclude that the uncertainty in the constriction width d is about 12 nm.

Figure 1(c) shows the temperature dependence of resistivity of the CrO_2 nanostructure with d=30 nm in the temperature range of 10 to 300 K. We convert the resistance data to resistivity in the nanostructure using the general-purpose simulation software COMSOL Multiphysics®. We observe that the resistivity decreases from 186.0 μ m cm at room temperature to 8.7 μ m cm at 10 K, yielding a large residue resistivity ratio $RRR = \frac{\rho_{300K}}{\rho_{10k}}$ of 21.5 which indicates a high crystalline quality of the nanostructure. As references, the RRR of a single crystal bulk CrO_2 is about 50 [18], and the RRR of high-quality epitaxial CrO_2 nanostructures is

typically in the range of 20 to 30 [2,13,19]. Based on the Boltzmann theory [18], we estimate the mean free path (MFP) at each temperature according to

$$l(T) \cong \frac{(2\pi)^3\hbar}{e^2} \frac{1}{A_{FS}^{\uparrow} + A_{FS}^{\downarrow}} \frac{3}{\rho(T)} \tag{1}$$

where A_{FS}^{\uparrow} and A_{FS}^{\downarrow} are Fermi surface areas of the majority and minority spins, respectively, $\rho(T)$ is the resistivity at temperature T, \hbar the reduced Plank constant, and e the elementary charge. According to band structure calculations of CrO_2 , $A_{FS}^{\uparrow} = 8.86 \text{ Å}^{-2}$ and $A_{FS}^{\downarrow} = 0$ [18]. The calculated mean free path l(T) is plotted in Fig. 1(c) in green and scaled against the right axis. The MFP increases from 18 Å at 300 K to 397 Å at 10 K. At 10 K, the MFP exceeds the constriction width d = 30 nm, and the electron transport becomes ballistic or at least quasiballistic. Note that in previous studies, device sizes are larger than the electron MFP and the electron transport is dissipative [2,13]. The MR behavior of spin textures in the half-metallic CrO_2 at the quantum transport regime is elusive and remains to be explored.

Figures. 2(a)-2(d) show the micromagnetic simulation results of the spin maps with domain walls created in the presence of proper reversing fields around constrictions with d = 30, 50, 120, and 200 nm, respectively. Away from a constriction, the nanostructure consists of two single domains (right versus left side) with spins along either +x or -x direction, respectively. Near each constriction, a DW complex is formed with varying details from one constriction to another, as represented by the color rendering and the color wheel (x-y plane). The white $(m_z = +1)$ and black $(m_z = -1)$ regions represent the out-of-plane spins. Figures 2(a)-2(d) show that the DWs locate on the left side of the constriction so that the demagnetization field due to DW is minimized. Spins inside the DWs rotate out-of-plane. Such DWs are known as Bloch walls

which tend to form when a film is thick. The contour of the DW is approximately a semioval. From Fig. 2(a) to Fig. 2(d), we observe that as the constriction width d gets smaller, the semioval DW contracts to be closer, or more localized, to the constriction, and moreover, the spin curvature in the constriction gets larger. The right column of maps in Figs. 2(a)-2(d) show the magnified spin maps near the constrictions. At the smallest d = 30 nm, spins rotate by about 90° across the constriction, where spins on the left of the constriction aligns mostly along y axis while spins on the right side of the constriction aligns along x axis. Contrastingly, at the largest d = 200 nm, spins are mostly aligned along the +x direction across the constriction with little change in the spin curvature. Figure 2(e) shows the spatial gradient of spins along the x axis, i.e., the spin curvature $\nabla \theta_x$, in the constriction, versus the constriction width d, where θ is the angle from the x-axis in the x-y plane. From d = 200 to 30 nm, the spin curvature at the center of the constriction increases from 0.008/nm to 0.025/nm. This indicates that the DW configuration is very sensitive to the constriction size. The tinier the constriction is, the larger spin curvature appears. Note that the spin curvature around the constrictions as shown in the right column of Figs. 2(a)-2(d) has a major implication on the magneto-transport as the narrowest region contributes most to the resistance. This can be inferred from the calculations of the electric potential distributions in Fig. 3 which is simulated through a two-dimensional model of a nanostructure with d = 30 nm using the COMSOL Multiphysics modeling software.

We generate and annihilate DWs in the nanostructures through applying moderate reversing magnetic fields. Figures 4(a)-4(d) show the field dependent resistance change relative to the zero-field resistance, $\Delta R = R(B) - R(0)$, and the corresponding magnetoresistance MR = $\frac{R(B) - R(0)}{R(0)}$, at d = 30, 50, 120, and 200 nm, respectively. Using Fig. 4(a), in which d = 30 nm, as an example, we specify the magnetization reversal and corresponding MR hysteresis loop as

follows. Initiating at -500 Oe, the whole nanostructure has its magnetization along the -x direction. We start to measure the resistance from -500 to 0 Oe, reaching point A. Reversing the field to the +x direction and increasing the field to 110 Oe (point A'), the overall spin curvature of the nanostructure increases for lowering the Zeeman energy. Consequently, the resistance increases continuously with the external field due to the spin curvature induced resistance as reported in our previous work [2]. When the magnetic field increases to 136 Oe (point B'), magnetization on the left side of the constriction reverses, creating a DW as shown in Fig. 2(a). When the magnetic field continues to increase to 156 Oe (point C'), the magnetization on the right side of the constriction is reversed to the +x direction. The DW is annihilated, and the resistance drops precipitously. As the magnetic field further increases to +500 Oe, the resistance decreases continuously with increasing field due to the decrease of the spin curvature. We denote the abrupt increase in resistance due to the appearance of a DW (from point A' to point B') as $\Delta R_{B'-A'}$. There seems to be some intermediate states between A' and B' at d = 30 nm, which has not been observed in other nanostructures. We speculate that when d = 30 nm, the MR is highly sensitive to the DW configuration and a slight change in the spin state manifests itself in MR. Figures 4(b)-4(d) show the similar magneto-transport behaviors, indicating the existence of the process of the DW creation and annihilation as in Fig. 4(a), for constrictions of d = 50, 120, and 200 nm, respectively.

To estimate the DWR at zero field, we perform the "half-hysteresis loop" measurement as shown in Fig. 5. Similar to the full loop measurement, we start the measurement from +500 Oe, where the magnetization in the wire is initialized along the +x direction, and then decrease the field to zero reaching point A. From 0 Oe (point A) to -138 Oe (point A'), an external field antiparallel to the sample's magnetization is applied. When the external field increases to -140

Oe (point B'), the DW is created. Instead of further increasing the magnetic field to wipe out the DW as in Fig. 4, we slowly decrease the magnetic field back to zero field (point B). The resistance change at zero field is $\Delta R_{\rm B-A}$. In our previous study, we have analyzed that the contributions from other MR effects apart from the DWR to the resistance change at zero field is negligible [13]. Therefore, ΔR_{B-A} can be considered as the resistance change induced by the creation of a magnetic DW. However, this type of measurement is not easy to implement when d is large because DW exists in a narrow range of the magnetic field. Fortunately, we notice that in Fig. 5, the resistance change from point A' to point B' is close to that from point A to point B. As mentioned before, the resistance changes from A to A' and from B to B' is due to the change of spin curvature in response to the external field. In the asymmetrical weak link design as shown in Fig. 1(a), spin curvature change arises mostly from the non-uniform region with angled wedges. Consequently, the spin curvature induced MR is dominated by spins on the right side of the constriction because the right side of the constriction contributes most to the measured resistance due to the small width and large length, as shown in Fig. 3. The spin curvature variation in this region is similar from A to A' and B to B' which is inferred from the fact that the creation or annihilation of the DW has little effect on the magnetization on the right side of the constriction. As a result, $\Delta R_{B'-A'} \approx \Delta R_{B-A}$, and $\Delta R_{B'-A'}$ is therefore a good measure of the DWR.

We obtain $\Delta R_{B'-A'}$ in all nanostructures with different constriction widths d from Figs. 4(a)-4(d). For each sample, $\Delta R_{B'-A'}$ is derived from the average of multiple measurements. From d=200 to 30 nm, $\Delta R_{B'-A'}$ increases from 0.6 m Ω to 42 m Ω by 70 folds. The corresponding MR = $\Delta R_{B'-A'}/R_0$ increases from 0.0075% to 0.36% by 48 folds. In Fig. 6, we plot the DWR ratio, $\Delta R_{B'-A'}/R_0$, versus the constriction width d, in a log-log scale. The horizontal error bars

represent the uncertainties in constriction widths as estimated from the SEM images. The vertical error bars are derived from the standard deviation of multiple measurements. The dashed line is a fitting to the data with $\Delta R_{B'-A'}/R_0$ proportional to $d^{-1.87\pm0.32}$. This result indicates that the DMR of our nanostructures is highly sensitive to the dimension of the constriction. The DWR is dramatically enhanced through reducing the constriction size.

Levy and Zhang's study calculates the DWR originating from the spin mixing of two spin current channels inside the DW in the diffusive transport regime. When the current flows perpendicular to the DW, the corresponding DWR is estimated to be

$$R_{\text{CPW}} = \frac{\xi^2}{5} \frac{(\rho_0^{\uparrow} - \rho_0^{\downarrow})^2}{\rho_0^{\uparrow} \rho_0^{\downarrow}} \left(3 + \frac{10\sqrt{\rho_0^{\uparrow} \rho_0^{\downarrow}}}{\rho_0^{\uparrow} + \rho_0^{\downarrow}} \right), \tag{2}$$

where ρ_0^{\uparrow} and ρ_0^{\downarrow} are resistivities for the spin up and spin down states, respectively, and $\xi \equiv \pi \hbar^2 k_F/4m\lambda J$ in which J donates the exchange splitting, m is the electron mass, and λ is the DW width.

Contrastingly, in a highly constricted nanostructure, when the spin flip MFP is much larger than the DW width such that electrons cannot accommodate the spin change across the constriction adiabatically, the ballistic MR (BMR) effect occurs. The magnitude of BMR is approximately

$$\frac{\Delta R}{R} (\%) = \frac{2P^2}{1 - P^2} F(P, \lambda) \tag{3}$$

where P is the spin polarization at the Fermi level, $F(P,\lambda)$ is the function showing the accommodation of spins inside the DW [20-24]. When the DW width λ is comparable with the

Fermi wavelength λ_F , $F(P,\lambda)$ behaves as $\exp(-\beta\lambda)$. When $\lambda \gg \lambda_F$, which is the case in our study, $F(P,\lambda)$ behaves as $\frac{1}{\alpha\lambda^2}$ [20-22,24], where β and α are constants. Both Eq. (2) and Eq. (3) show that the MR depends on the DW width through λ^{-2} . Note that in these theoretical studies, a standard DW configuration is adopted in calculations, where the DW width λ essentially characterizes the spin curvature inside the DWs. Contrastingly, a DW complex including the semioval DW and spin textures in the constriction as shown in Figs. 2(a)-2(d) forms our nanostructures. The spin curvature in nano-constrictions, which corresponds to the DW width in Eq. (2) and Eq. (3), as shown in Fig. 2(e) is expected to be the main source for the DWR as it is located in the narrowest region. The smaller the constriction width, the larger the spin curvature and the larger the DWR.

According to the power law with the exponent of -1.87±0.32, If the cross-sectional area of the CrO₂ nanostructure is reduced to 150 nm², e.g., in a 10 nm-thick film with a 15-nm wide constriction, the corresponding MR would reach approximately 100%. In comparison, Lepadatu et.al., predicted that the MR would be enhanced to about 70% in Ni and 30% in NiFe when the cross-sectional area is reduced to 1 nm² which is so small to be practical in fabrication [25]. The cross-sectional area of 150 nm² is much more feasible and the predicted large MR of 100% in a simple nanostructure of CrO₂ is a testament of the enhanced magneto transport of half metals. The DW confined by the geometry can be taken advantage of as an element for applications in magnetic sensing and information storage devices.

In conclusion, we have investigated the excess resistance induced by a single magnetic DW in a one-dimensional half-metallic CrO_2 nanoscale conductor with a built-in constriction with a variable channel width ranging from 30 to 200 nm. The purpose of the constriction is to

localize the magnetic DW in its vicinity, so that an external magnetic field can be applied to generate and annihilate the single magnetic DW. We have uncovered a large size effect of the DWR ratio on the constriction width d, $\Delta R/R_0 \propto d^{-1.87\pm0.32}$. Accordingly, we predict that the MR ratio of a simple CrO_2 nanowire impregnated with a constriction at a 150 nm² cross-section could reach 100%. This large MR far exceeds that of a conventional ferromagnetic nanowire, confirming the role of half metallicity on enhanced magneto transport. Based on this study, we conclude that the most effective method to increase the DW induced MR is to reduce the constriction size, so that the DW is localized to as closer to the constriction as possible. Our study suggests that magnetic domain structures are active electron transport agents and can be used to design highly functional half-metallic spintronic devices with enhanced performance.

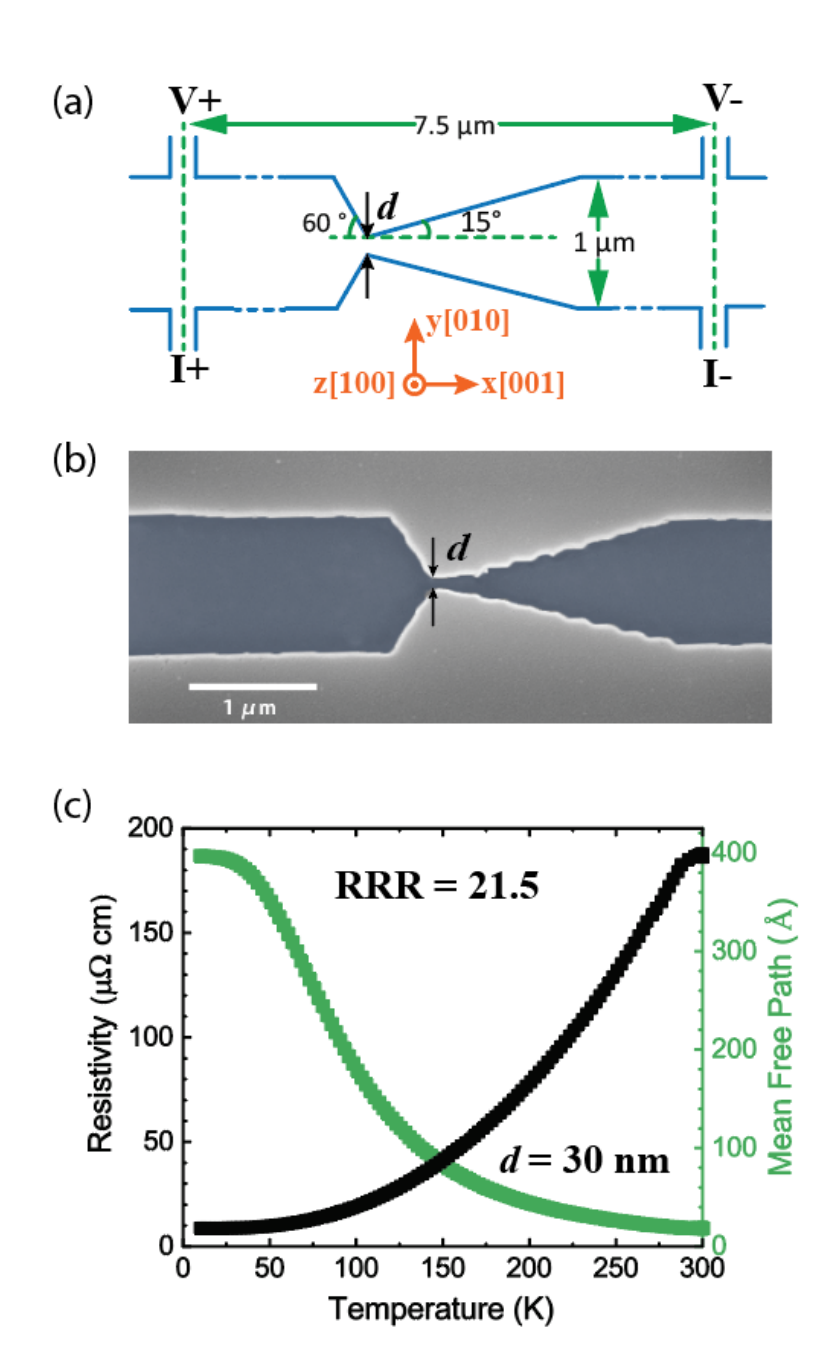


FIG. 1. (a) Schematic of a 100 nm-thick CrO_2 nanostructure with a constriction (neck) width d for magneto-transport measurement. The longitudinal axis of the wire is along the magnetocrystalline easy axis (x axis). (b) Scanning electron micrograph of an epitaxial CrO_2 nanostructure with d = 50 nm, where the dark region is CrO_2 and the light region is SiO_2 . (c) Temperature dependence of resistivity (black curve) and estimated electron mean free path (green curve) of an epitaxial CrO_2 nanostructure as shown in (a) with d = 30nm. The residual resistivity ratio (RRR), ρ_{300K}/ρ_{10K} , is 21.5.

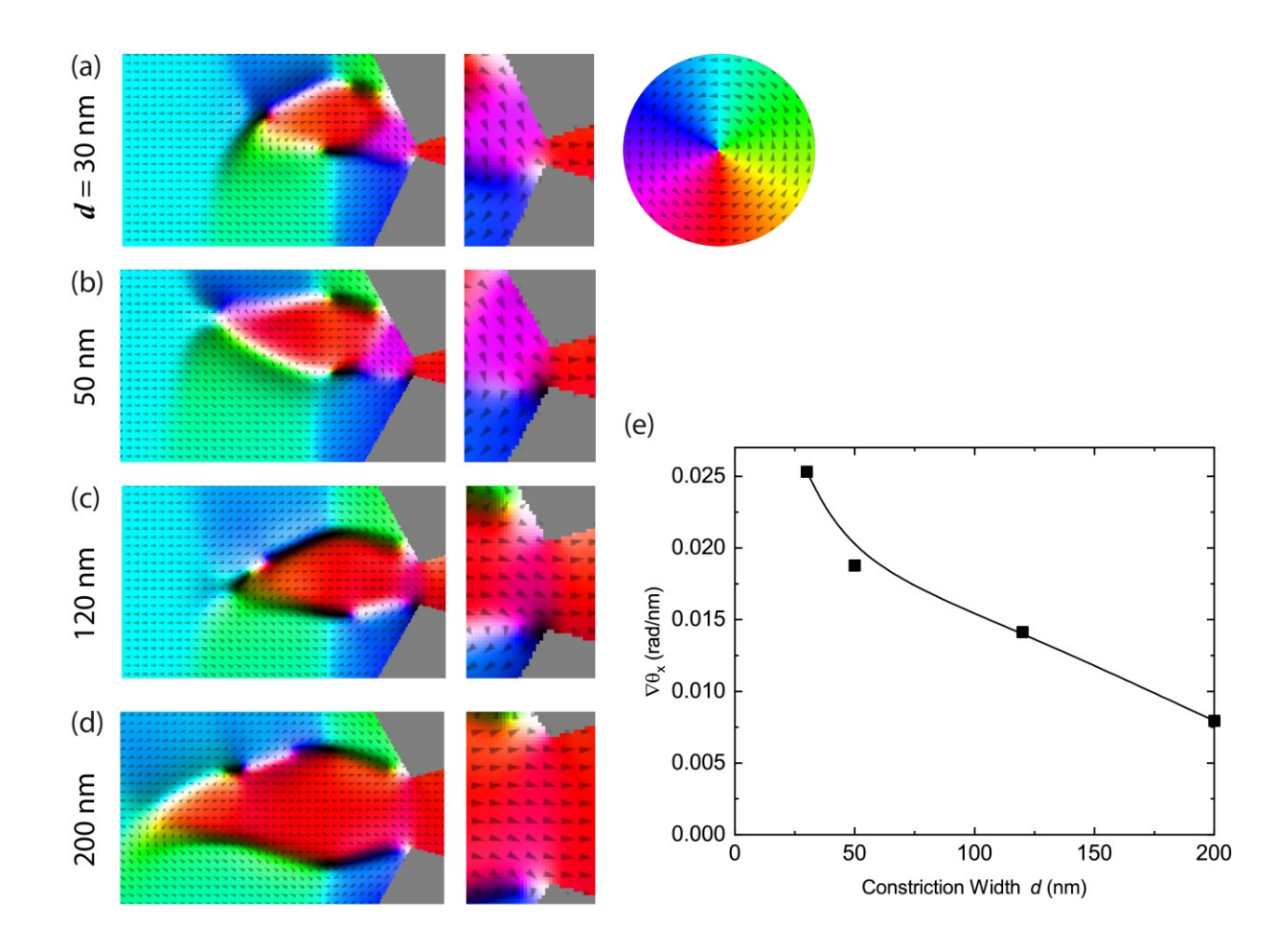


FIG. 2. (a)-(d) Micromagnetic simulation results of magnetic domain wall (DW) configurations in CrO_2 nanostructures with d=30, 50, 120, and 200 nm, respectively. The right column shows the detailed spin maps centered around the constrictions. The colors represent the magnetization direction. The x-y plane magnetization direction color map is shown in the color wheel. The brightness represents the out-of-plane magnetization contribution, where white and black corresponds to the upward (+z) and downward (-z) magnetization respectively. (e) The spatial gradient of spins along the x axis at the constriction, $\nabla \theta_x$, in nanostructures with different constriction widths d.

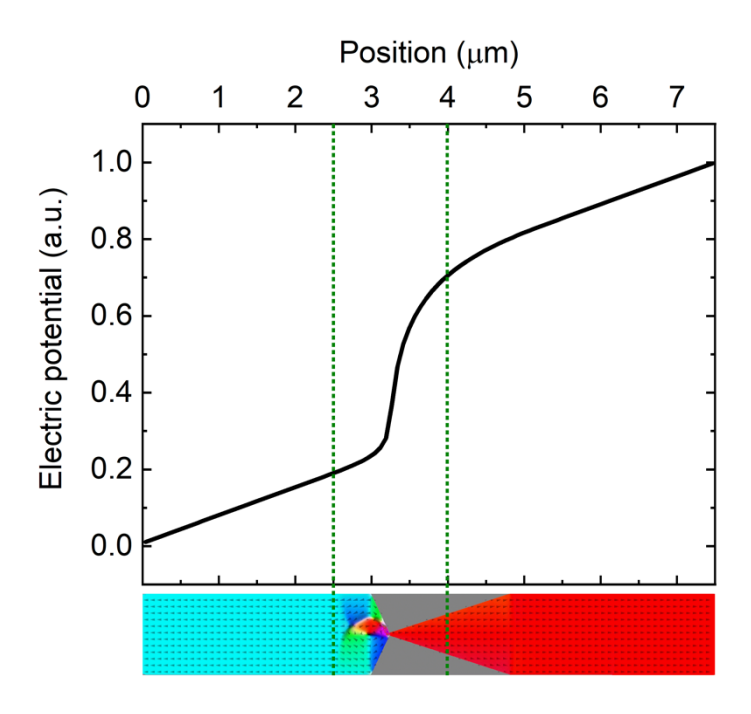


FIG.3. Electric potential distribution of the CrO_2 nanostructure with d = 30 nm simulated using the COMSOL Multiphysics modeling software. The electric potential has been normalized. It shows that the narrowest region contributes most to the resistance.

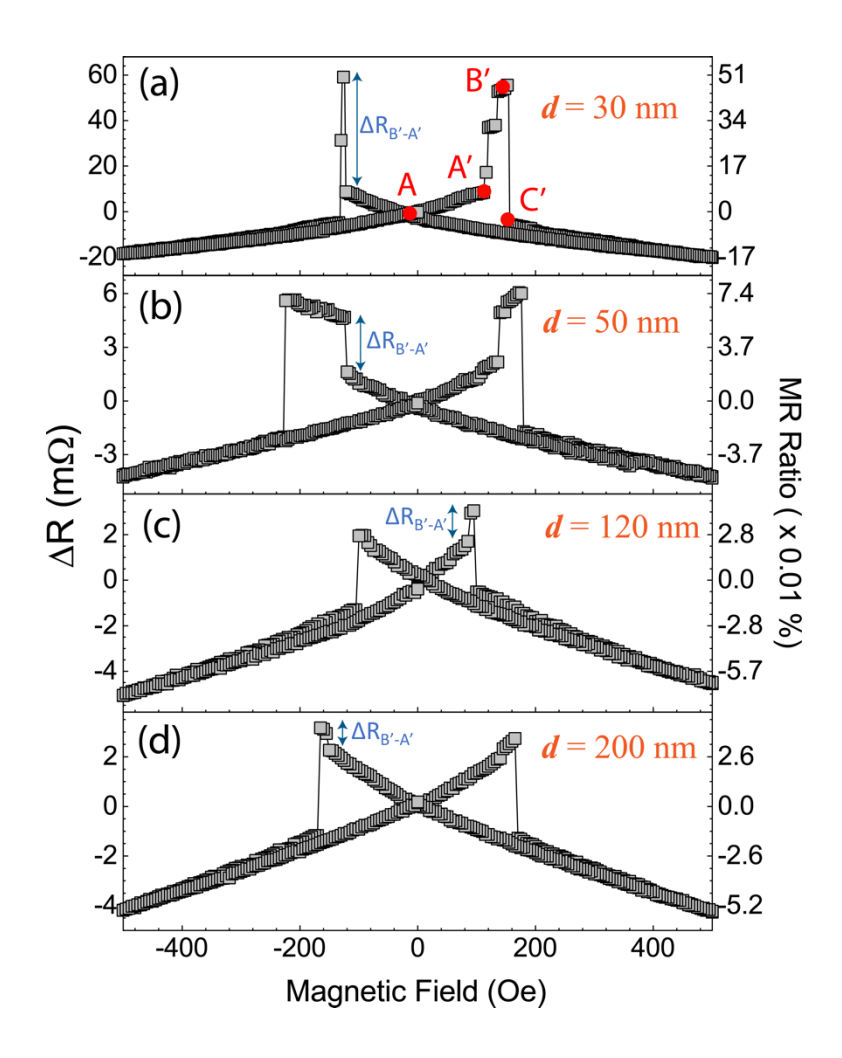


FIG. 4. (a)-(d) Magnetic field induced resistance change and magnetoresistance (MR) relative to zero-field resistance in CrO_2 nanostructures with d = 30, 50, 120, and 200 nm, respectively, at T = 10 K. When the external magnetic field increases, the resistance increases abruptly (from point A' to point B') due to the creation of a domain wall (DW). The corresponding resistance change upon domain wall generation is denoted as $\Delta R_{B'-A'}$.

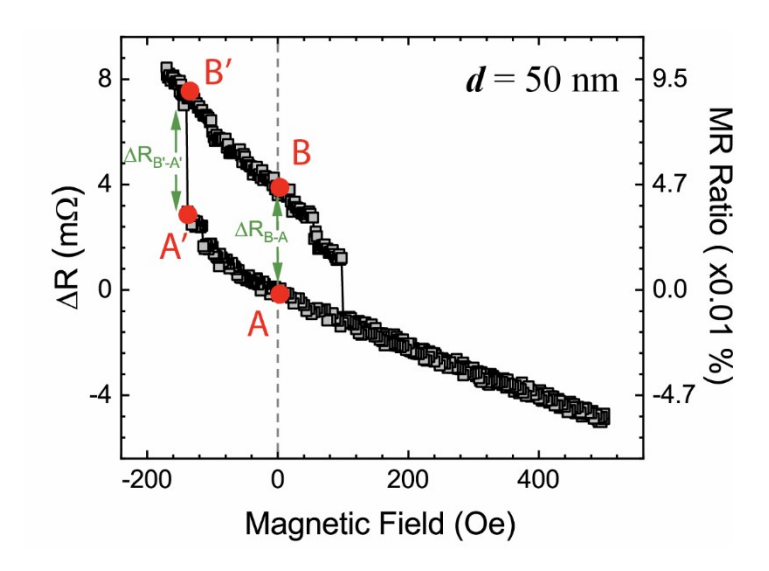


FIG. 5. Magnetic field induced resistance change and magnetoresistance (MR) relative to zero-field resistance in CrO_2 nanostructures with d = 50 nm at T = 10 K. Point A represents the resistance without domain wall (DW) at zero field. Point A' represents the resistance without DW at -140 Oe field. Point B' is state with DW at -140 Oe. Point B is the state with DW at zero field. ΔR_{B-A} is the zero-field DWR. $\Delta R_{B'-A'}$ is the DWR at -140 Oe field, which is the same as the $\Delta R_{B'-A'}$ denoted in FIG. 6.

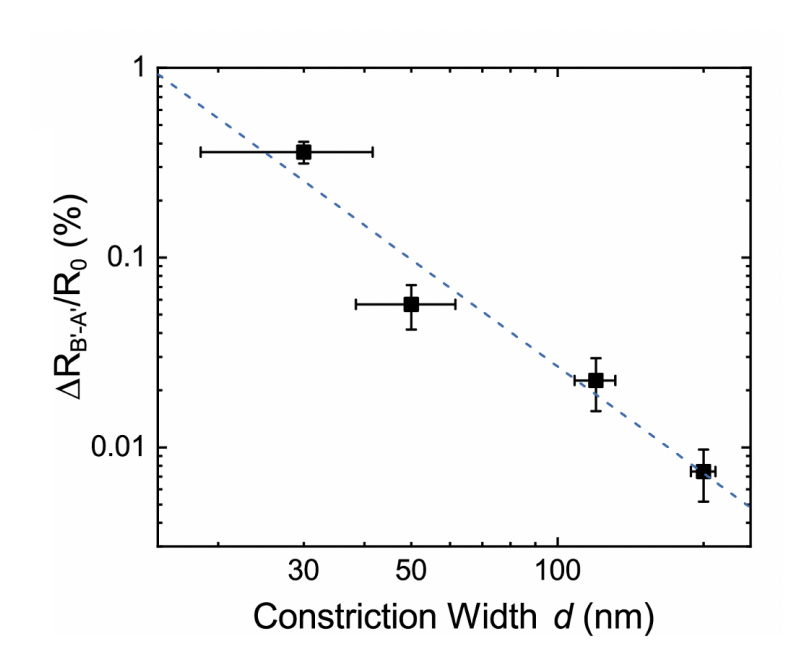


FIG. 6. $\Delta R_{B'-A'}/R_0$ versus constriction width d, plotted in a log-log scale. The dashed line is a power fit to the experimental results.

References:

- [1] P. M. Levy and S. Zhang, Physical Review Letters **79**, 5110 (1997).
- [2] L. Qian, W. Chen, and G. Xiao, Nanoscale **12**, 3958 (2020).
- [3] U. Ebels, A. Radulescu, Y. Henry, L. Piraux, and K. Ounadjela, Physical review letters **84**, 983 (2000).
- [4] D. Buntinx, S. Brems, A. Volodin, K. Temst, and C. Van Haesendonck, Physical review letters **94**, 017204 (2005).
- [5] G. Taylor, A. Isin, and R. Coleman, Physical Review **165**, 621 (1968).
- [6] J. Gregg, W. Allen, K. Ounadjela, M. Viret, M. Hehn, S. Thompson, and J. Coey, Physical Review Letters **77**, 1580 (1996).
- [7] S. S. Parkin, M. Hayashi, and L. Thomas, Science **320**, 190 (2008).
- [8] D. A. Allwood, G. Xiong, C. Faulkner, D. Atkinson, D. Petit, and R. Cowburn, Science **309**, 1688 (2005).
- [9] Y. Ji, G. Strijkers, F. Yang, C. Chien, J. Byers, A. Anguelouch, G. Xiao, and A. Gupta, Physical Review Letters **86**, 5585 (2001).
- [10] K. Schwarz, Journal of Physics F: Metal Physics 16, L211 (1986).
- [11] L. Chioncel, H. Allmaier, E. Arrigoni, A. Yamasaki, M. Daghofer, M. Katsnelson, and A. Lichtenstein, Physical Review B **75**, 140406 (2007).
- [12] J. Parker, S. Watts, P. Ivanov, and P. Xiong, Physical review letters 88, 196601 (2002).
- [13] W. Chen, L. Qian, and G. Xiao, Physical Review B **98**, 174402 (2018).
- [14] A. Vansteenkiste, J. Leliaert, M. Dvornik, F. Garcia-Sanchez, and B. Van Waeyenberge, CAS Article.
- [15] G. Miao, G. Xiao, and A. Gupta, Physical Review B **71**, 094418 (2005).
- [16] A. Biehler, M. Kläui, M. Fonin, C. König, G. Güntherodt, and U. Rüdiger, Physical Review B **75**, 184427 (2007).
- [17] P. Lubitz, M. Rubinstein, M. Osofsky, B. Nadgorny, R. Soulen, K. Bussmann, and A. Gupta, Journal of Applied Physics **89**, 6695 (2001).
- [18] S. P. Lewis, P. B. Allen, and T. Sasaki, Physical Review B **55**, 10253 (1997).
- [19] M. Rabe, J. Pommer, K. Samm, B. Özyilmaz, C. König, M. Fraune, U. Rüdiger, G. Güntherodt, S. Senz, and D. Hesse, Journal of Physics: Condensed Matter **14**, 7 (2001).
- [20] G. Tatara and H. Fukuyama, Journal of the Physical Society of Japan 63, 2538 (1994).
- [21] G. Tatara, Y.-W. Zhao, M. Munoz, and N. Garcia, Physical Review Letters 83, 2030 (1999).
- [22] G. Cabrera and L. Falicov, physica status solidi (b) 61, 539 (1974).
- [23] J. B. van Hoof, K. M. Schep, A. Brataas, G. E. Bauer, and P. J. Kelly, Physical Review B **59**, 138 (1999).
- [24] S. Chung, M. Munoz, N. Garcia, W. Egelhoff, and R. Gomez, Physical review letters **89**, 287203 (2002).
- [25] S. Lepadatu and Y. Xu, Physical review letters **92**, 127201 (2004).